Electrophoretic Deposition of Au Nanocrystals inside Perpendicular Mesochannels of TiO_2

Mehul N. Patel,[†] Ryan D. Williams,[‡] R. Alan May,[‡] Hiroshi Uchida,[§] Keith J. Stevenson,*[,‡] and Keith P. Johnston*[,†]

Department of Chemical Engineering and Department of Chemistry and Biochemistry, Center for Nano- and Molecular Science and Technology, Texas Materials Institute, The University of Texas at Austin, Austin, Texas 78712, and Department of Chemistry, Sophia University, Tokyo, Japan 102-8554

Received May 9, 2008. Revised Manuscript Received July 18, 2008

Au nanocrystals stabilized by dodecanethiol were deposited into 100−150 nm thick TiO_2 films with evenly spaced perpendicular nanopillars and mesochannels on the order of 10 nm supported on conducting ITO/glass electrodes. Electrophoretic deposition was used to enhance nanocrystal deposition within the mesoporous TiO_2 film. X-ray photoelectron spectroscopy (XPS), scanning electron microscopy with energy-dispersive X-ray (EDX), UV−vis spectroscopy, variable-angle spectroscopic ellipsometry (VASE), and scanning surface potential microscopy (SSPM) were used to characterize the resulting Au nanocrystal/TiO_2 composites. Au nanocrystal loadings reached 21 wt % and were not kinetically limited at 10 min, relative to depositions performed for 20 h. Both VASE measurements of the anisotropy of the imaginary refractive index, *k*, and X-ray photoelectron spectroscopy (XPS) depth profiling studies indicate that Au nanocrystals are dispersed within the vertically aligned mesopores and distributed throughout the film. The mean penetration depth of a single nanocrystal penetrating inside the film is described with a model in terms of the electric field and a local deposition rate constant, which is influenced by ligand binding and architecture on the nanocrystal surface.

Introduction

Titanium dioxide has been widely used in solar cells,[1] sensors,[2] batteries,[3] and photocatalysis.[4] Tuning of the mesoporous structure and composition of TiO_2 has been explored as a means to tailor optical, magnetic, photonic, electronic, and catalytic properties.[5] For instance, mesoporous TiO_2 has been shown to be a more effective catalyst because of its large surface area and pore structure that result in increased surface reactivity and improved mass transport. The facile preparation of ordered mesoporous electrodes with uniformly sized pores that are oriented perpendicular to the substrate are desirable for facilitating charge-transfer and mass transport.[6] Unfortunately, most synthetic strategies that use structure directing templates for preparing mesoporous TiO_2 films produce pore architectures with large pore size distributions with pores that are either tortuous in nature or that run parallel to the substrate.[7−12] In sol−gel synthesis of TiO_2 films using structure-directing block copolymers, the ratio of surfactant, metal oxide precursor, and solvent may be adjusted to control the morphology, pore size, and pore orientation.[13−16] This route involves evaporation-induced self-assembly (EISA),[17−20] where the film geometry begins to form as the growth substrate is withdrawn from a solution

* Corresponding author: (F):512-471-7060, (T): 512-471-4617, E-mail: kpj@che.utexas.edu, Corresponding author: (F):512-471-8696, (T): 512-232-9160, E-mail: stevenson@cm.utexas.edu.

[†] Department of Chemical Engineering, The University of Texas at Austin.

[‡] Texas Materials Institute, The University of Texas at Austin.

[§] Sophia University.

(1) Gratzel, M. *Nature* **2001**, *414* (6861), 338–344.
(2) Iwanaga, T.; Hyodo, T.; Shimizu, Y.; Egashira, M. *Sens. Actuators, B* **2003**, *B93* (1−3), 519–525.
(3) Long, J. W.; Dunn, B.; Rolison, D. R.; White, H. S. *Chem. Rev.* **2004**, *104* (10), 4463–4492.
(4) Huang, S. Y.; Kavan, L.; Exnar, I.; Graetzel, M. *J. Electrochem. Soc.* **1995**, *142* (9), L142–L144.
(5) Guliants, V. V.; Carreon, M. A.; Lin, Y. S. *J. Membr. Sci.* **2004**, *235* (1−2), 53–72.
(6) Etienne, M.; Grosso, D.; Boissiere, C.; Sanchez, C.; Walcarius, A. *Chem. Commun.* **2005**, (36), 4566–4568.
(7) Alberius, P. C. A.; Frindell, K. L.; Hayward, R. C.; Kramer, E. J.; Stucky, G. D.; Chmelka, B. F. *Chem. Mater.* **2002**, *14* (8), 3284–3294.
(8) Wang, K.; Yao, B.; Morris, M. A.; Holmes, J. D. *Chem. Mater.* **2005**, *17* (19), 4825–4831.
(9) Crepaldi, E. L.; de Soler-Illia, G. J.; Grosso, D.; Cagnol, F.; Ribot, F.; Sanchez, C. *J. Am. Chem. Soc.* **2003**, *125* (32), 9770–9786.
(10) Carreon, M. A.; Choi, S. Y.; Mamak, M.; Chopra, N.; Ozin, G. A. *J. Mater. Chem.* **2007**, *17* (1), 82–89.
(11) Choi, S. Y.; Mamak, M.; Coombs, N.; Chopra, N.; Ozin, G. A. *Adv. Funct. Mater.* **2004**, *14* (4), 335–344.
(12) Grosso, D.; Soler-Illia, G. J. d. A. A.; Babonneau, F.; Sanchez, C.; Albouy, P.-A.; Brunet-Bruneau, A.; Balkenende, A. R. *Adv.Mater.* **2001**, *13* (14), 1085–1090.
(13) Boettcher, S. W.; Fan, J.; Tsung, C.-K.; Shi, Q.; Stucky, G. D. *Acc. Chem. Res.* **2007**, *40* (9), 784–792.
(14) Grosso, D.; Soler-Illia, G. J. d. A. A.; Crepaldi, E. L.; Cagnol, F.; Sinturel, C.; Bourgeois, A.; Brunet-Bruneau, A.; Amenitsch, H.; Albouy, P. A.; Sanchez, C. *Chem. Mater.* **2003**, *15* (24), 4562–4570.
(15) Sanchez, C.; Boissiere, C.; Grosso, D.; Laberty, C.; Nicole, L. *Chem. Mater.* **2008**, *20* (3), 682–737.
(16) Lancelle-Beltran, E.; Prene, P.; Boscher, C.; Belleville, P.; Buvat, P.; Lambert, S.; Guillet, F.; Boissiere, C.; Grosso, D.; Sanchez, C. *Chem. Mater.* **2006**, *18* (26), 6152–6156.
(17) Lu, Y.; Ganguli, R.; Drewien, C. A.; Anderson, M. T.; Brinker, C. J.; Gong, W.; Guo, Y.; Soyez, H.; Dunn, B.; Huang, M. H.; Zink, J. I. *Nature (London)* **1997**, *389* (6649), 364–368.
(18) Brinker, C. J.; Lu, Y.; Sellinger, A.; Fan, H. *Advanced Materials (Weinheim, Germany)* **1999**, *11* (7), 579–585.
(19) Cagnol, F.; Grosso, D.; Soler-Illia, G. J. d. A. A.; Crepaldi, E. L.; Babonneau, F.; Amenitsch, H.; Sanchez, C. *J. Mater. Chem.* **2003**, *13* (1), 61–66.

10.1021/cm8012705 CCC: $40.75
Published on Web 09/10/2008

containing both surfactant and metal oxide precursor. As the solvent evaporates, the local surfactant concentration increases to form micelles that guide the metal oxide precursor into hydrophilic regions to form phase-segregated regions. Our group and others have demonstrated that anatase mesoporous TiO_2 thin films with perpendicular pores can be prepared on polymer-modified glass,[21] silicon wafers,[22] and conducting ITO/glass substrates.[23] Similarly, Watkins and co-workers have prepared mesoporous silica films on silicon, by facilitating diffusion and condensation reactions with supercritical CO_2.[24]

The incorporation of nanocrystals such as Au, Pt, and Ag into mesoporous TiO_2 is known to enhance optoelectronic and catalytic properties.[25−30] Metal/semiconductor films have typically been prepared by reduction of metal ion precursors inside a mesoporous thin film by heat, electrochemical deposition, or UV radiation.[28,29,31−36] However, with these methods, it is difficult to control the nanocrystal morphology, size, and dispersion; furthermore, the nanocrystals may grow until they block the pores.[37] To better control the nanocrystal composition, size, and dispersion within mesoporous powders, a novel approach has been developed in which presynthesized nanocrystals are infused into the mesoporous support.[38−40] Several methods have been used to drive nanocrystal infusion including sonication[38] and the addition of a nonsolvent, supercritical CO_2, to an organic solvent such as toluene.[39,40] The $scCO_2$ strengthens the nanocrystal−mesoporous silica interaction leading to higher loadings. The stabilizing ligand may be designed to be removed at low temperatures after infusion.[40] This technique provides excellent control over the morphology of the mesoporous support as well as the nanocrystal size, shape, and composition for the purpose of achieving high catalytic activities and stabilities.[38,40]

An alternative approach to designing nanocomposite thin films is electrophoretic deposition of presynthesized nanocrystals on flat substrates such as carbon coated copper grids[41,42] and ITO/glass.[43,44] Kamat et al. have used this technique in organic solvents to deposit charged Au, Pt, and Ir nanocrystals onto films composed of disordered 10−40 nm TiO_2 nanocrystals.[26,27] The film thickness depends upon both the concentration and deposition time. Metal nanocrystal layers formed by electrophoretic deposition are generally thicker than those formed by Langmuir−Blodgett, self-assembled monolayer, or adsorption techniques. The aggregated nanocrystals form nanoporous films.[45] Thick films of CdSe nanocrystals deposited from an organic solvent, hexane, have been deposited electrophoretically onto conducting planar substrates composed of a 150 nm Au/10 nm Ti/Si wafer.[46−48] CdSe nanocrystals were also electrophoretically deposited selectively onto patterned Au films.[46,48] Electrophoretic deposition produced more uniform films than dry casting or spin casting.[46]

Very few studies report electrophoretic deposition of nanocrystals into mesoporous thin films. Preferably, the pores of the film should be perpendicular to the substrate and aligned with the electric field.[49,50] Limmer et al. have infused small nanoclusters inside porous membranes such as track-etched polycarbonate or anodic alumina with pore sizes of 100−200 nm and thicknesses to 10 μm.[51−54] The nanoclusters completely filled the pores of the membranes and were heated to form nanowires. Zhang et al. used electrophoretic deposition to infuse 3 nm CdSe nanocrystals into thin polymer films with 15 nm pores and a thickness of 30−40

(20) Grosso, D.; Cagnol, F.; Soler-Illia, G. J. D. A. A.; Crepaldi, E. L.; Amenitsch, H.; Brunet-Bruneau, A.; Bourgeois, A.; Sanchez, C. *Adv. Funct. Mater.* **2004**, *14* (4), 309–322.
(21) Koganti, V. R.; Dunphy, D.; Gowrishankar, V.; McGehee, M. D.; Li, X.; Wang, J.; Rankin, S. E. *Nano Lett.* **2006**, *6* (11), 2567–2570.
(22) Wu, C.-W.; Ohsuna, T.; Kuwabara, M.; Kuroda, K. *J. Am. Chem. Soc.* **2006**, *128* (14), 4544–4545.
(23) Uchida, H.; Patel, M. N.; May, R. A.; Gupta, G.; Stevenson, K. J.; Johnston, K. P. Perpendicularly-Oriented Mesoporous Titania Thin Films Prepared via Surfactant Assembly on Conductive Indium-Tin-Oxide/Glass Substrate. 2008, in preparation.
(24) Pai, R. A.; Humayun, R.; Schulberg, M. T.; Sengupta, A.; Sun, J.-N.; Watkins, J. J. *Science* **2004**, *303* (5657), 507–511.
(25) Kamat, P. V. *J. Phys. Chem. C* **2007**, *111* (7), 2834–2860.
(26) Chandrasekharan, N.; Kamat, P. V. *Nano Lett.* **2001**, *1* (2), 67–70.
(27) Subramanian, V.; Wolf, E.; Kamat, P. V. *J. Phys. Chem. B* **2001**, *105* (46), 11439–11446.
(28) Kumai, Y.; Tsukada, H.; Akimoto, Y.; Sugimoto, N.; Seno, Y.; Fukuoka, A.; Ichikawa, M.; Inagaki, S. *Adv. Mater.* **2006**, *18* (6), 760–762.
(29) Perez, M. D.; Otal, E.; Bilmes, S. A.; Soler-Illia, G. J. A. A.; Crepaldi, E. L.; Grosso, D.; Sanchez, C. Growth of Gold Nanoparticle Arrays in TiO2 Mesoporous Matrixes. *Langmuir* **2004**, *20* (16), 6879–6886.
(30) Cortial, G.; Siutkowski, M.; Goettmann, F.; Moores, A.; Boissiere, C.; Grosso, D.; Le Floch, P.; Sanchez, C. Metallic nanoparticles hosted in mesoporous oxide thin films for catalytic applications. *Small* **2006**, *2* (8−9), 1042–1045.
(31) Besson, S.; Gacoin, T.; Ricolleau, C.; Jacquiod, C.; Boilot, J.-P. *Nano Lett.* **2002**, *2* (4), 409–414.
(32) Gu, J.-L.; Shi, J.-L.; You, G.-J.; Xiong, L.-M.; Qian, S.-X.; Hua, Z.-L.; Chen, H.-R. *Adv. Mater.* **2005**, *17* (5), 557–560.
(33) Gu, J.; Xiong, L.; Shi, J.; Hua, Z.; Zhang, L.; Li, L. *J. Solid State Chem.* **2006**, *179* (4), 1060–1066.
(34) Bartl, M. H.; Boettcher, S. W.; Frindell, K. L.; Stucky, G. D. *Acc. Chem. Res.* **2005**, *38* (4), 263–271.
(35) Lee, U. H.; Lee, H.; Wen, S.; Mho, S.-i.; Kwon, Y.-U. *Microporous Mesoporous Mater.* **2006**, *88*, 48–55.
(36) Stathatos, E.; Lianos, P.; Falaras, P.; Siokou, A. *Langmuir* **2000**, *16* (5), 2398–2400.
(37) Rolison, D. R. *Science* **2003**, *299* (5613), 1698–1702.
(38) Rioux, R. M.; Song, H.; Hoefelmeyer, J. D.; Yang, P.; Somorjai, G. A. *J. Phys. Chem. B* **2005**, *109* (6), 2192–2202.
(39) Gupta, G.; Shah, P. S.; Zhang, X.; Saunders, A. E.; Korgel, B. A.; Johnston, K. P. *Chem. Mater.* **2005**, *17* (26), 6728–6738.
(40) Gupta, G.; Stowell, C. A.; Patel, M. N.; Gao, X.; Yacaman, M. J.; Korgel, B. A.; Johnston, K. P. *Chem. Mater.* **2006**, *18* (26), 6239–6249.
(41) Giersig, M.; Mulvaney, P. *Langmuir* **1993**, *9* (12), 3408–13.
(42) Giersig, M.; Mulvaney, P. *J. Phys. Chem.* **1993**, *97* (24), 6334–6.
(43) Trau, M.; Saville, D. A.; Aksay, I. A. *Science* **1996**, *272* (5262), 706–9.
(44) Bailey, R. C.; Stevenson, K. J.; Hupp, J. T. *Adv. Mater.* **2000**, *12* (24), 1930–1934.
(45) Chandrasekharan, N.; Kamat, P. V. *J. Phys. Chem. B* **2000**, *104* (46), 10851–10857.
(46) Islam, M. A.; Herman, I. P. *Appl. Phys. Lett.* **2002**, *80* (20), 3823–3825.
(47) Islam, M. A.; Xia, Y.; Steigerwald, M. L.; Yin, M.; Liu, Z.; O'Brien, S.; Levicky, R.; Herman, I. P. *Nano Lett.* **2003**, *3* (11), 1603–1606.
(48) Islam, M. A.; Xia, Y.; Telesca, D. A., Jr.; Steigerwald, M. L.; Herman, I. P. *Chem. Mater.* **2004**, *16* (1), 49–54.
(49) Hornyak, G.; Kroll, M.; Pugin, R.; Sawitowski, T.; Schmid, G.; Bovin, J.-O.; Karsson, G.; Hofmeister, H.; Hopfe, S. *Chem.−Eur. J.* **1997**, *3* (12), 1951–1956.
(50) Kamada, K.; Fukuda, H.; Maehara, K.; Yoshida, Y.; Nakai, M.; Hasuo, S.; Matsumoto, Y. *Electrochem. Solid-State Lett.* **2004**, *7* (8), B25–B28.
(51) Limmer, S. J.; Seraji, S.; Forbess, M. J.; Wu, Y.; Chou, T. P.; Nguyen, C.; Cao, G. *Adv. Mater.* **2001**, *13* (16), 1269–1272.
(52) Limmer, S. J.; Hubler, T. L.; Cao, G. *J. Sol−Gel Sci. Technol.* **2003**, *26* (1/2/3), 577–581.
(53) Limmer, S. J.; Cruz, S. V.; Cao, G. Z. *Appl. Phys. A: Mater. Sci. Process.* **2004**, *79* (3), 421–424.
(54) Limmer, S. J.; Chou, T. P.; Cao, G. Z. *J. Sol−Gel Sci. Technol.* **2005**, *36* (2), 183–195.

nm.[55] In both of these studies, the pore to nanocrystal diameter ratio, while a tunable feature, was greater than 5.

The objective of this study was to achieve high loadings and deep penetration of 3.1 nm Au nanocrystals into 10 nm perpendicular pores in ~150 nm thick mesoporous TiO_2 thin films supported on conducting ITO/glass electrodes. The effect of electrophoresis on the kinetics and thermodynamics of deposition is analyzed by comparison with control experiments without an applied electric field for deposition times of 10 min and 20 h. The electric field was varied as well as the nanocrystal concentration in the bulk phase. The electrical and structural properties of the prepared mesoporous TiO_2 thin films were characterized by scanning surface potential microscopy, atomic force microscopy, and scanning electron microscopy. UV−vis spectroscopy of the nanocomposite films was used to provide a relative measure of the nanocrystal loading. These loadings will be shown to be consistent with the absolute loadings determined by EDX and elemental analysis. Spectroscopic ellipsometry and X-ray photoelectron spectroscopy indicate that the Au nanocrystals penetrated deeply into the pores of the TiO_2 film with a maximum loading of 21% by weight and 12% by volume. The influence of the various properties including the nanocrystal size, pore diameter, electrophoretic mobility, electric field strength, and local deposition rate constant on the mean penetration depth of a single nanocrystal was analyzed based on an electrophoretic deposition model, which is based on the Fokker−Planck equation.[56,57] From the experimental mean deposition distance in the pores, a rate constant was estimated from the model. The penetration depth of the nanocrystals depends upon the strength of the nanocrystal-wall interactions, which are influenced by the coverage of the metal surface by the dodecanethiol ligands. The presynthesis of both the nanocrystals and the mesoporous thin films is shown to be a useful approach to control the nanocrystal shape, size, composition, and dispersion within the pores, as well as the mesoporous structure of the thin film.

Experimental Section

Materials. All chemicals were used as received. Titanium (IV) isopropoxide ($Ti(O\cdot i\text{-}C_3H_7)_4$) (97%), hydrogen tetrachloroaurate(III) trihydrate ($HAuCl_4\cdot 3H_2O$) (99.9%), tetraoctylammonium bromide ($(C_8H_{17})_4$-NBr) (98%), sodium borohydride ($NaBH_4$) (99%), and 1-dodecanethiol ($C_{12}H_{25}SH$) (98%) were purchased from Sigma-Aldrich Cooperation, and toluene (99.9%), chloroform (99.9%), hydrocholoric acid (HCl) (35.5%), ethanol (C_2H_5OH) (Absolute 200 proof), and 2-propanol ($(CH_3)_2CHOH$) (99.9%) from Fisher Scientific. Nonionic triblock copolymer surfactant Pluronic P123 (poly-(ethylene oxide) poly-(propylene oxide) poly-(ethylene oxide) EO_{20}-PO_{70}-EO_{20}) was supplied by BASF. Water (H_2O) was double-distilled and deionized. ITO/glass substrates were purchased from Delta Technologies, Limited.

Preparation of Substrates. The substrates for the mesoporous thin films were prepared as described elsewhere.[23] ITO/glass slides were cut into 1 × 1 cm^2 sections, rinsed using 2-propanol, and blown dry in air flow. A TiO_2 buffer layer was coated on the ITO/glass substrate by chemical solution deposition. The purpose of the buffer layer is to increase the surface energy of the substrate to facilitate self-assembly of the polymer micelles to template the mesoporous structure. Ti solution was prepared by mixing 0.03 g of $Ti(O\cdot i\text{-}C_3H_7)_4$ and 10 cm^3 of 2-propanol. ITO/glass substrates were dip-coated with a speed of ~ 6.0 cm/min, followed by heat-treatment at 200 °C for 5 min in air for drying and polymerization. The film thickness of the TiO_2 buffer layer was estimated to be approximately 2 nm by spectroscopic ellipsometry.[23]

Preparation of Mesoporous Titania Films. Mesoporous titania films were prepared by self-assembly of block copolymer surfactants in sol−gel solution as described elsewhere.[22,23] 1.05 g of $Ti(O\cdot i\text{-}C_3H_7)_4$ was hydrolyzed using 0.74 g of concentrated aqueous HCl under stirring for 10 min at room temperature. The hydrolyzed sol was mixed with 0.2 g of P123 surfactant dissolved in 3.0 g of ethanol while stirring for 15 min at room temperature. The resulting solution was spin-coated on the substrates at a rate of ~7500 rpm for 60 s, followed by aging at −10 °C for 2 days under a controlled humidity of ~45−55%. The samples were subsequently calcined using a tube furnace at 400 °C for 4 h in air with a heating rate of 1.0 °C/min to remove the block copolymer template and fix the mesoporous structure of the film.

Au Nanocrystal Synthesis. Au nanocrystals were synthesized by a two-phase arrested precipitation technique.[58,59] 15 mL of aqueous (0.064 M) hydrogen tetrachloroaurate(III) trihydrate ($HAuCl_4\cdot 3H_2O$) was combined with 25 mL of toluene solution containing 2.7 g of phase transfer catalyst, tetraoctylammonium bromide. After stirring for 1 h, the organic phase, with the transferred Au, was collected. The Au salt was then reduced using 15 mL of an aqueous sodium borohydride ($NaBH_4$) solution (0.44 M), resulting in Au nanocrystals dispersed in toluene, protected by the phase transfer catalyst. To this solution was added 0.240 mL of dodecanethiol 1 h later; stirring was continured for one more hour. The Au nanocrystals were washed and size-selected using ethanol as an antisolvent. Finally, the Au nanocrystals were dispersed in chloroform. The Au nanocrystals were 3.1 ± 0.7 nm as measured by transmission electron microscopy with 1.9 nm length dodecanethiol[60] capping ligands.

Au/TiO_2 Composite Formation. In the electrophoretic deposition process, the mesoporous TiO_2 on ITO/glass was the negative electrode. Electrical contact was made on the naked edge of the ITO substrate to ensure good electrical contact. The positive counter electrode was bare ITO/glass with the same dimensions. The electrodes were spaced 3 mm apart and completely immersed in a 2.5 mL Au nanocrystal dispersion (~0.1−0.2 mg/mL) in chloroform. A potential of 25 or 50 V was applied for 10 min to infuse the Au nanocrystals inside the mesoporous TiO_2 film. A control experiment was done by dipping the mesoporous TiO_2 film in the Au nanocrystal dispersion (~0.1 mg/mL) for 10 min and 20 h without an applied electric field. The Au nanocrystal dispersion showed no visual change in concentration (color) after nanocomposite formation, consistent with the very large number of nanocrystals in the bulk solution versus the small amount adsorbed.

Characterization. The microstructure of the mesoporous film was observed using a Zeiss Supra 40VP field emission scanning electron microscope (SEM). The SEM observation was performed at an accelerating voltage of 5−10 kV. UV−vis spectra were measured using a Varian Cary 5000 spectrophotometer. Scanning surface potential microscopy measurements of the mesoporous TiO_2

(55) Zhang, Q.; Xu, T.; Butterfield, D.; Misner, M. J.; Ryu, D. Y.; Emrick, T.; Russell, T. P. *Nano Lett.* **2005**, *5* (2), 357–361.
(56) Haber, S.; Gal-Or, L. *J. Electrochem. Soc.* **1992**, *139* (4), 1071–8.
(57) Haber, S. *J. Colloid Interface Sci.* **1996**, *179* (2), 380–390.
(58) Brust, M.; Walker, M.; Bethell, D.; Schiffrin, D. J.; Whyman, R. *J. Chem. Soc., Chem. Commun.* **1994**, (7), 801–2.
(59) Brust, M.; Fink, J.; Bethell, D.; Schiffrin, D. J.; Kiely, C. *J. Chem. Soc., Chem. Commun.* **1995**, (16), 1655–6.
(60) Aslam, M.; Mulla, I. S.; Vijayamohanan, K. *Appl. Phys. Lett.* **2001**, *79* (5), 689–691.

were performed on a Veeco Bioscope Atomic Force Microscope (AFM) with a Nanoscope IV controller. Scan sizes were 1 × 1 μm, and the scan rate was 1 Hz. The interleave scan used for surface potential measurements was fixed at 10 nm.[61] Potentials were applied to the mesoporous film by connecting the ITO support to the sample stage with conductive Cu tape. The SSPM probes used for data collection were custom fabricated from NSC15/Ti−Pt (Mikromasch) Pt coated AFM probes. Previous experiments have shown these probes have insufficient resolution for nanoscale SSPM studies,[62,63] so they were modified in a dual-beam focused ion beam (FEI DB235) with a 30 keV beam and beam current of 20 nA. Cone angles of the probes were reduced from 30 to 10°, and tip radii were unchanged.

X-ray photoelectron spectroscopy was done with a PHI 5700 XPS system using a monochromatic Al X-ray source. The system was calibrated using Au4f, Ag3d, and Cu2p peaks. Ar ions at 3 kV and a 45° angle were used to sputter the sample for a known length of time. The sample was measured with XPS for Au and Ti after each sputtering time. The bottom of the film was defined as the point where a large increase in the amount of In was detected. Energy dispersive X-ray analysis was performed using a LEO 1530 SEM equipped with an IXRF EDX system, the latter operated with a 20 kV electron beam and 60 μm aperture (average counts ~2000 s^{-1}). Elemental analysis was done with a Varian GTA120 AA240-Z graphite tube atomizer. Nanocomposites were dissolved in aqua regia overnight. The solution containing Au ions was then analyzed to determine the Au content.

A J. A. Woolam M-2000 variable-angle spectroscopic ellipsometer was used to determine the ellipsometry parameters Ψ and Δ from 200 to 800 nm at three different angles, 60, 65, and 70°. The same instrument was also used to record p-polarized transmission measurements from 300 to 800 nm. To extract the film thickness as well as the real (n) and imaginary (k) portion of the complex refractive index, we fit the data using a three-layer model consisting of a glass substrate, indium tin oxide,[64] and the film layer. As described previously,[23] mesoporous TiO_2 was modeled assuming isotropic optical constants with a Tauc−Lorentz (T−L) oscillator for the band gap and two additional Gaussian oscillators. Upon Au infusion, this isotropic approximation did not adequately describe the ellipsometry and transmission data. As a result an anisotropic uniaxial model was used to model the TiO_2 films following Au infusion. The ordinary (x-y plane) portion of the uniaxial model used a T−L oscillator[65] for the band gap, a large Gaussian above the band gap whose tail also accounted for small Urbach absorption below the band gap, a Gaussian in the visible describing the Au plasmon band, and finally a Drude oscillator[66] accounting for broad free carrier type adsorption. The extreme (z plane) refractive index used the same T−L oscillator with a Gaussian above the band gap but absorption in the visible was modeled with only a Drude oscillator. A more complex description of the extreme absorption was not necessary, and the simple two-variable Drude model is desirable because of the large number of fit parameters already present in the model.

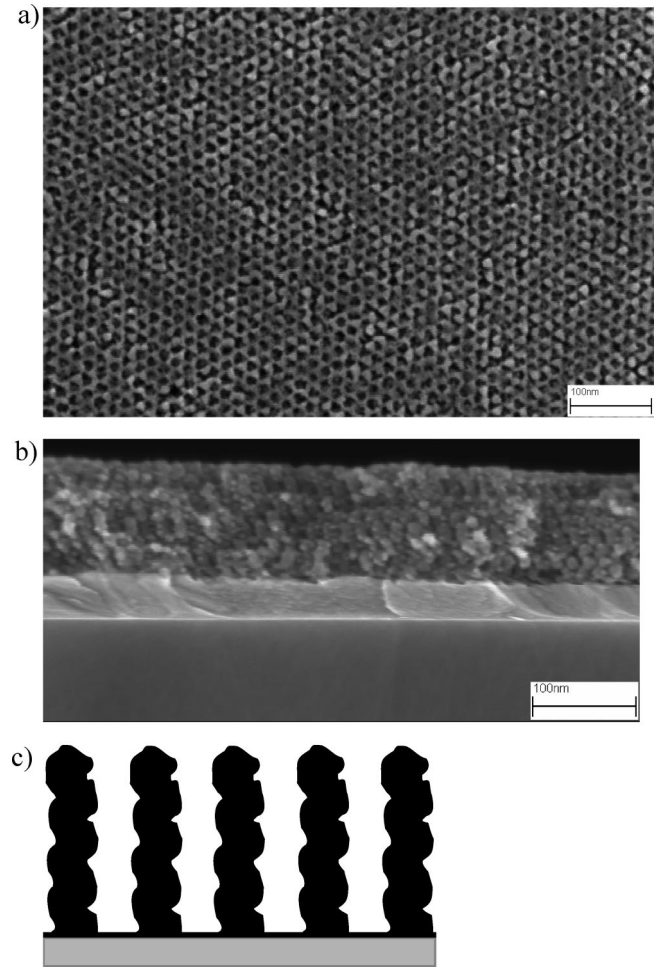

Figure 1. SEM image of ~110 nm mesoporous TiO_2 thin film on ITO/glass with 10 ± 2 nm pores and 10 ± 2 nm pillars. (a) Top down view. (b) Cross-section view. (c) Schematic of perpendicular nanopillars on ITO/glass.

Results

Figure 1 shows a SEM image of the mesoporous TiO_2 films with a hexagonal close-packed geometry. The top down view in Figure 1a shows ~10 nm pores spaced apart by ~10 nm nanopillars on a TiO_2 buffered ITO/glass substrate. The inverse mesospace (pores) and nanopillars run perpendicular to the ITO conducting substrate as seen in the cross-section view of Figure 1b and the schematic of Figure 1c. Evenly spaced pillars are present with a continuous void space. The film thickness ranges from ~100−150 nm. The layer underneath the TiO_2 film is the conducting ITO, which is approximately 60−100 nm thick as indicated by the manufacturers.

To gain insight into the electrical properties of the TiO_2 film without any Au, we performed scanning surface potential microscopy to determine the potential drop across the TiO_2 film. The AFM topography scan in Figure 2a resembles the structure seen in the SEM image (Figure 1a). The underlying ITO substrate was connected to an external voltage source and potentials of 0.0, 5.0, and 10.0 V were applied. Measured surface potentials were within 1% of the applied potential, thus the TiO_2 did not appreciably reduce the applied bias as shown in crossectional surface potential

(61) McMurray, H. N.; Williams, G. *J. Appl. Phys.* **2002**, *91* (3), 1673–1679.
(62) Jacobs, H. O.; Leuchtmann, P.; Homan, O. J.; Stemmer, A. *J. Appl. Phys.* **1998**, *84* (3), 1168–1173.
(63) Williams, R. D.; Stevenson, K. J. Unpublished results.
(64) May, R. A.; Kondrachova, L.; Hahn, B. P.; Stevenson, K. J. *J. Phys. Chem. C* **2007**, *111* (49), 18251–18257.
(65) Jellison, G. E., Jr.; Modine, F. A. *Appl. Phys. Lett.* **1996**, *69* (3), 371–373.
(66) Tompkins, H. G.; McGahan, W. A., *Spectroscopic Ellipsometry and Reflectometry*; Wiley-Interscience: New York, 1999.

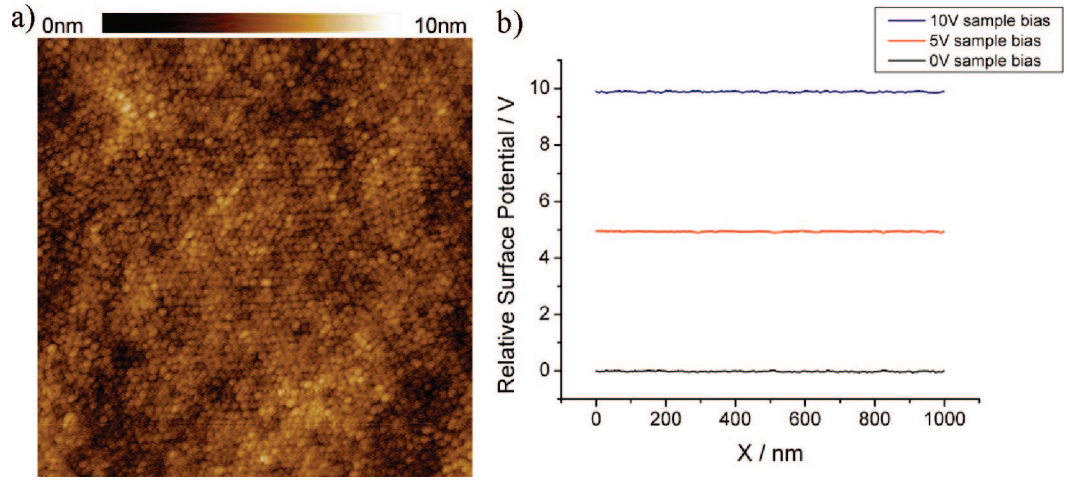

Figure 2. (a) 1 × 1 μm^2 AFM topography image of the TiO_2 surface structure. (b) Cross-sectional line plots of surface potential measured across TiO_2 surface. Only a 1% error between the potential measured at the TiO_2 surface and that applied to the underlying ITO substrate indicates that the TiO_2 film had very little effect on the electrophoretic fields used for the Au nanocrystal insertion.

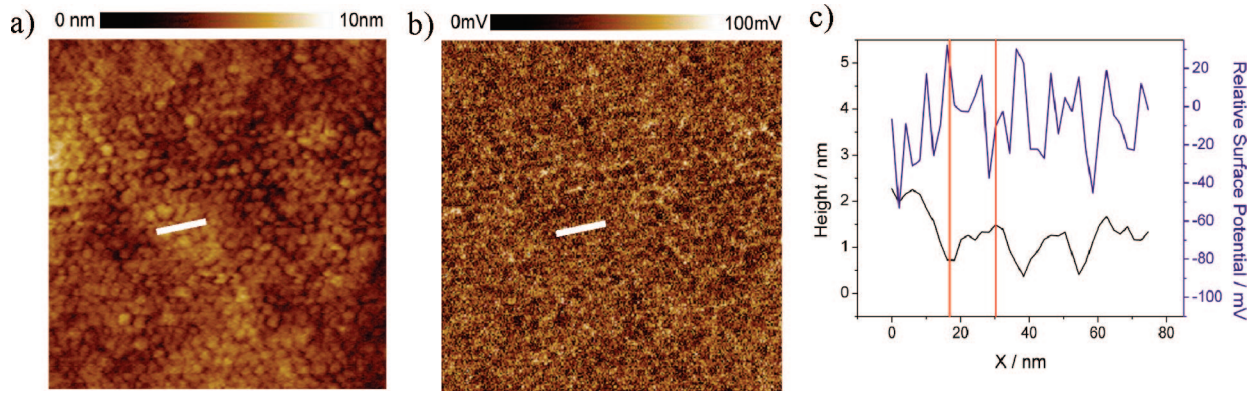

Figure 3. (a) 500 × 500 nm^2 AFM topography image of Au/TiO_2 nanocomposite. (b) 500 × 500 nm^2 surface potential image of (a) shows clear resolution of the porous structure. (c) Data from the line indicated in (a) and (b) show typical potential differences (blue line) between the pore and the pillars (black line) of the Au/TiO_2 nanocomposite.

line scans (Figure 2b). This suggests that there is no large ohmic drop that would signify a highly resistive TiO_2 film. These small potential drops indicate that there is very little difference between the applied potential applied to the ITO electrode and the measured potential at the top of the TiO_2 film.

Although the measured surface potentials were similar to the applied potential on large scales, nanoscale potential differences due to the porous symmetry of the film could not be resolved with conventional AFM probes. These potential differences, although very small in magnitude in comparison to the large potentials applied to the sample, are important to understand as they may influence Au nanocrystal transport within the mesoporous TiO_2 film. The determination of potential differences on such small size scales is not possible with conventional probe geometries,[67,68] because they have a large tip diameter (~30 nm) and a cone angle of approximately 30°. This large tip diameter and cone angle leads to a large averaging effect in surface potential imaging and greatly reduces the resolution of the measurement.[62,63]

Successful imaging of the minute differences in surface potential along the surface of the TiO_2 required an AFM probe with a much smaller cone angle. To obtain the desired geometry, we milled the probes in a focused ion beam (FIB) to a resulting cone angle of 10° with a tip radius ≤20 nm. Although the topographical resolution was very similar to that obtained with conventional Pt coated probes (Figure 3a), surface potential sensitivity was improved significantly. The mesoporous symmetry of the TiO_2 was clearly visible in the surface potential images, where potential differences between the mesopores and pore walls were typically 50 mV (Figure 3b). SSPM imaging of the Au/TiO_2 nanocomposite with no applied potential bias (0 V) showed surface potentials that were 50−90 mV higher in the mesopores relative to the pore walls (Figure 3c). Presumably, this potential difference was found to be influenced by the addition of the Au nanocrystals in the pores because TiO_2 films without Au exhibit a potential difference between pores and pillars of the film below the noise floor of 12 mV (see the Supporting Information, Figure S1).

UV−vis spectroscopy of the Au/TiO_2 films is shown in Figure 4. The spectra have been normalized to an absorbance of 0 at 720 nm to aid visual comparison. A peak at ~515 nm is clearly present associated with the surface plasmon

(67) Zerweck, U.; Loppacher, C.; Otto, T.; Grafstroem, S.; Eng, L. M. *Phys. Rev. B: Condens. Matter Mater. Phys.* **2005**, *71* (12), 125424/1–125424/9.
(68) Jacobs, H. O.; Knapp, H. F.; Mueller, S.; Stemmer, A. *Ultramicroscopy* **1997**, *69* (1), 39–49.

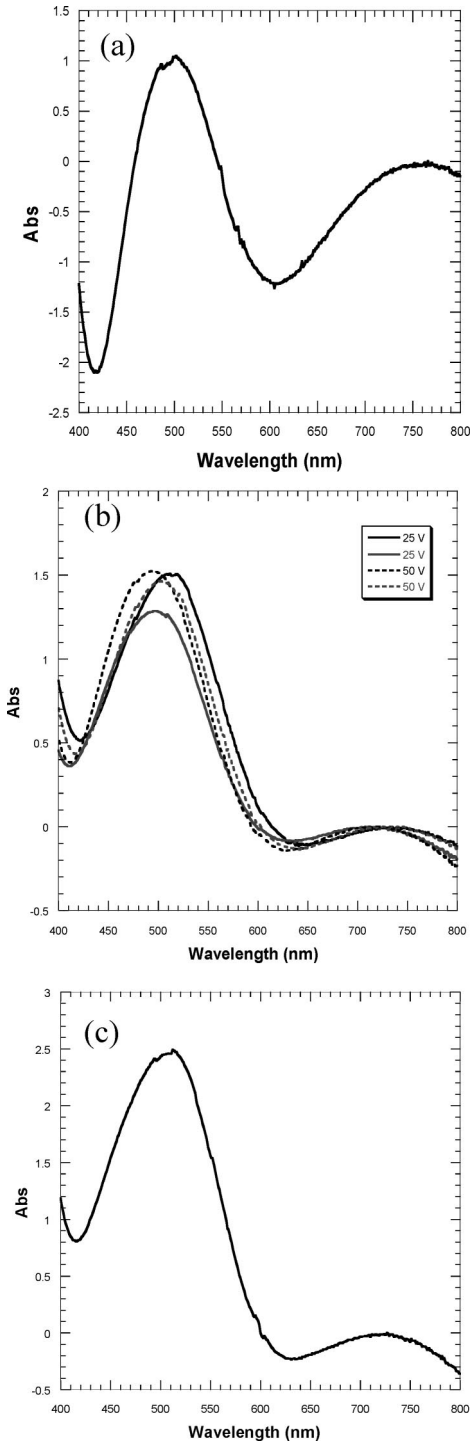

Figure 4. UV−vis spectroscopy of Au/TiO_2 nanocomposites. Experimental conditions: (a) ∼0.1 mg/mL, 20 h, 0 V; (b) ∼0.1 mg/mL, 10 min, 25 or 50 V; and (c) ∼0.2 mg/mL, 10 min, 25 V.

resonance (SPR) of Au. As shown in Figure 4a and Table 1, control experiments without an applied field at 10 min. and 20 h gave the lowest absorbances of 0.987 and 1.05, respectively. The similar absorbance values indicated that the nanocrystal incorporation was not kinetically limited over 10 min, but thermodynamically limited. Figure 4a shows a control experiment in which the absorbance spectrum for Au/TiO_2 composite assembled by immersion for 20 h without an applied voltage exhibits a peak of diminished absorbance at 502 nm corresponding to roughly a 33% decrease in absorbance relative to Au/TiO_2 composites assembled with

Table 1. Maximum Absorbance for Surface Plasmon Resonance of Au for Initial Au Concentration of 0.1 mg/mL and 10 min Deposition Time

	max abs
control (0 V)	0.987
control (0 V)[a]	1.05
25 V	1.4 ± 0.2
50 V	1.50 ± 0.04
25 V[b]	2.49

[a] Deposition time was 20 h. [b] Initial Au nanocrystal concentration = 0.2 mg/mL.

Table 2. Au Loading As Determined by SEM EDX and Elemental Analysis for Initial Au Concentration of 0.1 mg/mL and 10 min Deposition Time

	SEM EDX (wt %)	elemental analysis (wt %)	vol %
control (0 V)	4 ± 1		1.9
control (0 V)[a]	4.6 ± 0.5	4.7	2.3
25 V	12 ± 2	7.9	4.0
50 V	9 ± 3	8.2	4.1
25 V[b]	21 ± 5		12

[a] Deposition time was 20 h. [b] Initial Au nanocrystal concentration = 0.2 mg/mL.

an applied electric field (Figure 4b). Very similar results were obtained in 10 min without an applied voltage. Brownian motion led to significant deposition, but less than in the electrophoretic deposition experiments with an applied field. Figure 4b shows the spectra for Au nanocrystals deposited electrophoretically at two different electric field strengths, 83 and 167 V/cm, corresponding to 25 and 50 V, respectively. There was a slight increase in the maximum absorbance on doubling the electric field, as shown in Table 1. Increasing the nanocrystal dispersion concentration by approximately a factor of 2 nearly doubled the maximum absorbance in the nanocomposite as shown in Figure 4c and Table 1 at a given field of 83 V/cm. Also the amount of nanocrystals loaded in each case was less than 2% of the total number of nanocrystals in bulk, so that the concentration of nanocrystals in the solution can be assumed to be constant.

The complicated oscillating absorbance spectrum, which is most prevalent in Figure 4a with the lowest Au deposition, is attributed to interference effects occurring from the multiple interfaces comprising the ordered mesoporous film. The interfaces between the TiO_2, ITO, and glass produce interference fringes leading to the oscillations in the absorbance even with no Au present (see the Supporting Information, Figure S2). Small shifts of the SPR can also be seen in the spectra and can be attributed either to the slight changes in the relative dielectric constant in the immediate vicinity of the nanocrystal or to the interference effects from the films.

SEM EDX and elemental analysis of the Au/TiO_2 nanocomposite films were utilized to further quantify the nanocrystal loadings for a constant nanocrystal concentration of 0.1 mg/mL. As shown in Table 2, the values from SEM EDX are slightly higher than those obtained from elemental analysis, but are within experimental error for two of the three conditions. The control experiment without an applied potential gave the lowest amount of Au incorporation with a loading of ∼4 wt % by SEM EDX for 10 min and ∼4.6 wt % by SEM EDX and ∼4.7 wt % by elemental analysis for 20 h, where wt % reflects the amount of Au relative to the total weight of Au and TiO_2. In comparison pore filling

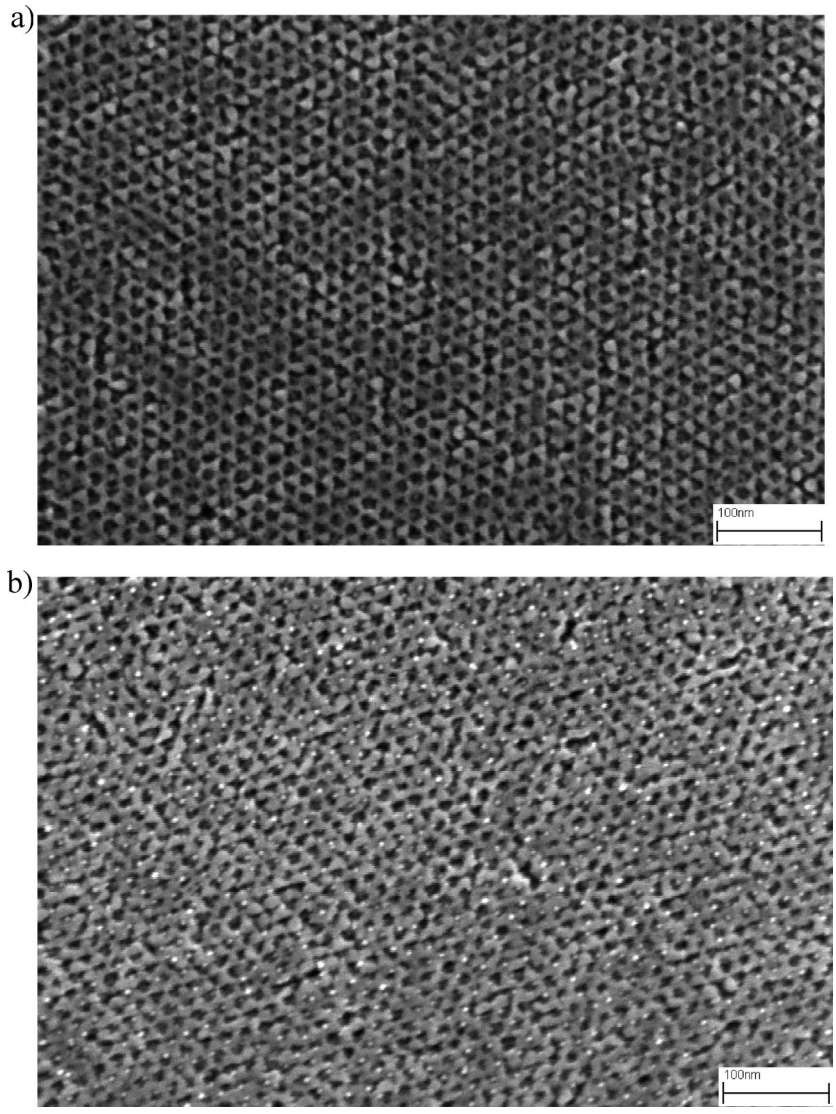

Figure 5. SEM top down view of (a) mesoporous TiO_2 and (b) Au/TiO_2 nanocomposite.

for the control experiments led to Au loadings of 1.9 and 2.3 vol %, respectively, where vol % is volume of Au over the film pore volume. The SEM EDX data for the control experiment further corroborate that the loadings are thermodynamically limited and not kinetically limited as nanocrystal adsorption reaches equilibrium in 10 min. The loadings were comparable for the nanocomposites made by electrophoretic deposition at the two electric field strengths of 83 and 167 V/cm, on the order of 8 wt % (~4.0 vol %). The small effect of doubling the electric field confirmed the results from UV−vis spectroscopy (Figure 4 and Table 1). For the more concentrated Au dispersion (0.2 mg/mL), the loading reached ~21 wt % Au according to SEM EDX at 83 V/cm. With this highest loading, the amount of pore volume occupied is 12 vol %. The ratio of loadings at 0.2 versus 0.1 mg/mL dispersion was comparable with a ratio of ~1.7 from SEM EDX and ~1.8 from the absorbance maxima from UV−vis spectroscopy.

A top down view SEM image of the Au/TiO_2 nanocomposite film is given in Figure 5b. The empty porous TiO_2 film is provided in Figure 5a for easier comparison with the synthesized Au/TiO_2 nanocomposite. The Au nanocrystals are evenly dispersed across the TiO_2 film. The depth of field is limited by the short working distance of the microscope making it difficult to image deep within the pores. Thus, this orientation does not provide depth resolution for these nanocrystals with respect to the mesopores. In Figure 5a, the mesopores of the film are seen as dark spots. In Figure 5b, the pores of the film are not as dark, possibly indicating the presence of Au nanocrystals within the pores. The nanocrystals in the image retain their size and shape after electrophoretic deposition without aggregation. The SEM images were very similar for nanocomposites produced by electrophoretic deposition and adsorption without an electric field. The nanocrystal diameter in Figure 5b is 3.7 ± 0.8 nm. This size is only slightly larger than the as-synthesized nanocrystal size of 3.1 ± 0.7 nm and is attributed to the difficulty in sizing the nanocrystals from the image due to the blurred edges.

The films were further characterized by variable-angle spectroscopic ellipsometry. Despite the anisotropic geometry of the columnar mesoporous TiO_2, good model fits of ellipsometric and transmission data have been obtained by assuming isotropic films, that is, the same optical constants regardless of orientation.[23] However, for Au infused films,

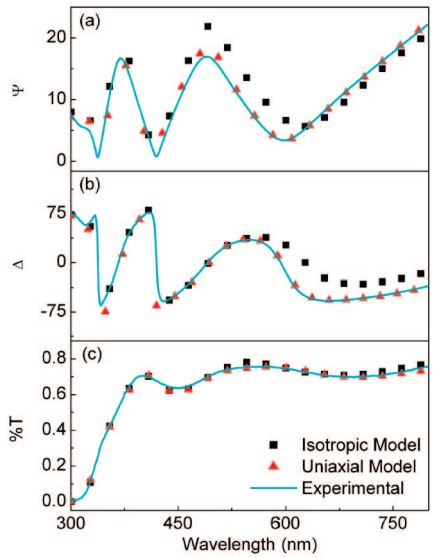

Figure 6. (a) Ψ, (b) Δ, and (c) %T experimental (line) and model fits (symbols) for best fit isotropic (square) and uniaxial (triangle) models of mesoporous TiO_2 infused with 21 wt % Au. The misfit of the isotropic model in the visible region justifies the inclusion of anisotropy using the more complex uniaxial model.

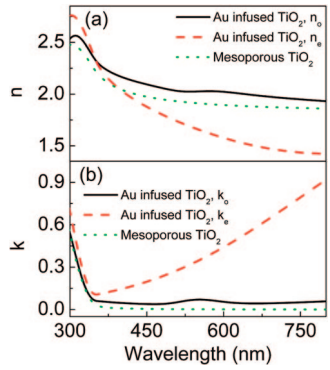

Figure 7. (a) Real and (b) imaginary components of the complex refractive index for mesoporous TiO_2 (green dots) as well as the normal (solid) and extreme (red dash) refractive index of mesoporous TiO_2 infused with 21 wt % Au. The large k_e in the visible spectrum indicates alignment of the Au particles along the film's z axis.

the best fit isotropic model is unsatisfactory and overestimates Ψ from ∼450 to 650 nm and Δ from ∼570 to 800 nm (Figure 6). A uniaxial anisotropic model, in which the film's z axis has different optical constants than the x and y axis, remedies this problem resulting in good fits across the spectral range. The extracted optical constants (Figure 7) provide insight into how Au is loaded into the film. Mesoporous TiO_2 behaves like a classic semiconductor with no absorption and normal dispersion before the band gap and a sharp increase in absorbance in the UV corresponding to a band gap transition. Following infusion of ∼21 wt % Au the ordinary, $x-y$ plane, optical constants (n_o and k_o) of the film are similar to those found before infusion with the addition of a plasmon absorbance at ∼550 nm and a small broad absorbance extending out into the near IR (Figure 7b). This extra absorbance shifts n_o upward because of the Kramers−Kronig relationship (Figure 7a). A similar attenuation of absorbance in the visible to near IR was observed by Granqvist and Hunderi[69] for individually isolated 3−4 nm Au nanocrystals.

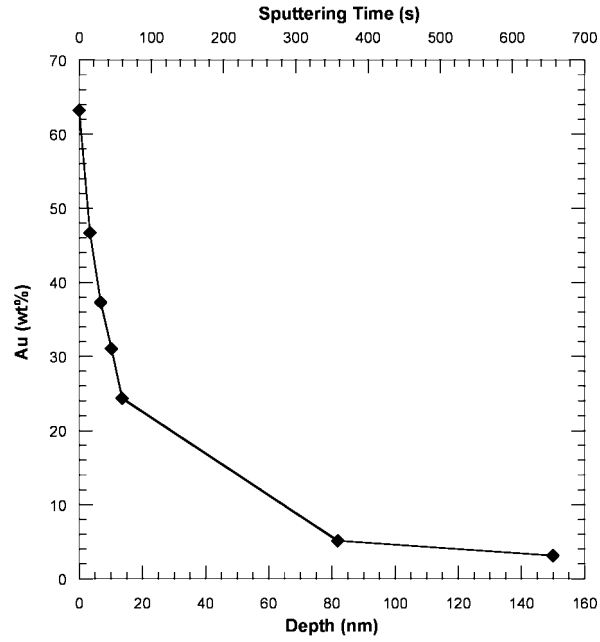

Figure 8. Au 4f XPS depth profiling experiment. Plot of Au wt % versus sputtering time and depth for 21 wt % Au in mesoporous TiO_2 thin film.

The extreme (z plane) imaginary refractive index, k_e, is significantly enhanced compared to the weak absorbance, small k_o, of the x-y plane (Figure 7b). This large absorbance in the visible to near IR arises from free electron absorbance due to the formation of a conduction band by overlapping orbitals, indicating that the Au nanocrystals are in close contact.[69] From these observations two important conclusions are reached. First, the lack of absorbance in the $x-y$ plane means that any residual Au nanocrystals on the TiO_2 surface are so dispersed that they are not in contact with each other. This corroborates SEM data that indicate that very few nanocrystals are located on the surface and implies that most of the Au detected by elemental analysis and EDX is packed into the TiO_2 mesopores. Inside the mesopores the small pore diameter limits lateral contact between the nanocrystals in the $x-y$ plane. Second, the large absorbance in the z direction means that light oriented in this direction "sees" more of the free electron absorption associated with nanocrystals in contact with one another. Because the z direction is oriented with the film's columnar mesopores, the obvious conclusion is that the Au nanocrystals are loaded vertically into the pores.

XPS was performed on the 21 wt % Au/TiO_2 nanocomposite film. Figure 8 shows the Au concentration as a function of sputtering time and film depth. The sample was sputtered for a certain length of time and the Au concentration was measured relative to the Ti concentration. A simple linear correlation between sputtering time and the film thickness was used to generate the depth profile. The time where a sharp increase in the indium concentration occurred was used as the time at which the film bottom was reached. Many of the Au nanocrystals reside near the top half of the mesoporous TiO_2 film. The Au concentration steadily decreases with film depth. Although there are a significant

(69) Granqvist, C. G.; Hunderi, O. *Phys. Rev. B* **1977**, *16* (8), 3513–34.

number of Au nanocrystals near the bottom of the film, this value could be inflated by small amounts of Au being forced downward into the film by the sputtering process. The average Au concentration throughout the film thickness was ~20 wt % in good agreement with the SEM EDX value of 21 wt %.

Discussion

A significant amount of nanocrystals were adsorbed onto the TiO_2 surface even in the absence of an applied potential. This loading was caused by the interaction between the nanocrystals and TiO_2 surface along with rapid diffusion through the pores due to the high ratio of the film's internal surface area to the top surface area (~26). This adsorption is over an order of magnitude larger than for similar dodecanethiol coated nanocrystals into mesoporous silica particles.[39] The greater adsorption is facilitated by the stronger interaction of the nanocrystals with TiO_2. Higher activities have also been reported for Au/TiO_2 relative to Au/SiO_2 for CO oxidation[70,71] implying that the interaction of Au with TiO_2 is stronger than Au with SiO_2. The increase in nanocrystal loading with the application of an electric field may be caused by: (1) an increase in the local nanocrystal concentration at the pore entrance produced by electrophoresis, (2) a change in the nanocrystal-TiO_2 interaction based on the surface charge on the TiO_2, or (3) deeper penetration into the pores caused by an enhancement in the electrophoretic velocity in the pores. The SSPM measurements suggest that the pores of the TiO_2 film extend throughout the length of the film thickness, as the surface potential measured across the pores is slightly larger as compared to the pore walls. The electric field in the pores described by this gradient can produce electrophoresis within the pores.

Theoretical calculations of a close-packed surface coverage of a monolayer of nanocrystals on the top planar TiO_2 film surface will now be used to show that the majority of the nanocrystals are contained within the pores. From an analysis of Figure 1, the area fraction of voids on the top surface of the film is ~30%. Consequently, the top planar surface area for the pillars is 1.7 m^2/g TiO_2 for a film thickness of 150 nm. For 3.1 nm diameter Au nanocrystals, the area/g of a nanocrystal is 25 m^2/g Au. A close-packed monolayer with a packing density of 0.907 (2D hexagonal) of Au nanocrystals on the top planar surface of TiO_2 would correspond to a loading of 5.9 wt %, or equivalently, ~9 nanocrystals on top of each pillar. The highest experimental loading (~21 wt %) was more than three times greater than this close-packed value. Moreover, Figure 5b indicates the amount of Au on the top planar film surface of ~0.3 wt % Au is far below the close-packed value, and the VASE results also indicate that the nanocrystals are dispersed in the pores of the film. Hence, the vast majority of nanocrystals are within the pores and not on the top surface.

The experimental loading may be compared with the theoretical loading for a monolayer of Au nanocrystals on each pillar. For films with ~ 8 wt % (4.0 vol %, relative to the film pore volume) and ~21 wt % (12 vol %) Au loading, there would be ~30 and ~90 nanocrystals, respectively, around each pillar, if all of the nanocrystals were associated directly with a pillar. These values were estimated by dividing the total number of nanocrystals by the number of pillars. These 90 nanocrystals would cover ~15% of the pillar surface area, excluding the surface area on top of the pillar. The nanocrystals inside the film are closer together than this value of 15% in the *z*-direction, but not along the nanopillar circumference. Assuming a maximum packing fraction of 74 vol% for spheres inside of the void volume of the film (porosity = 30% from Figure 1), the maximum loading would be 62 wt % Au, corresponding to ~560 nanocrystals per pillar. With the ~10 nm gap between pillars, not all of the nanocrystals would be required to be directly on a pillar. For example another 4 nm would be available between two pillars after attaching two 3.1 nm nanocrystals directly on the pillars. Of the estimated 560 nanocrystals around each pillar, ~470 would be directly attached to the pillar surface (62 vol % of the max. 74 vol % packing in the total void volume) and ~90 would be found in the annular region (12 vol %). Hence, even with the experimental number of nanocrystals adsorbed directly onto the pillars, there exists sufficient space for more nanocrystals to access the pores of the film. The tortuosity of the pores may be expected to inhibit nanocrystals from reaching the film bottom, although diffusion in the circumferential direction for the interconnected annuli is favorable. Thus, the apparent thermodynamic limit after 10 min is likely not the true thermodynamic limit for perfect nanopillar geometry. XPS shows that the distribution of nanocrystals favors the upper regions of the film.

The motivation for using a low dielectric constant (ε) nonpolar organic solvent in this study was several-fold. In a polar solvent such as water or ethanol, the charge on the surface of a Au nanocrystal may be achieved more readily, and the higher ε favors a higher electrophoretic mobility. However, the nanocrystal size of Au may be controlled more precisely for synthesis in nonpolar solvents.[58] Furthermore, both positive and negatively charged nanocrystals may be present simultaneously in low ε organic solvents. Also, electrochemical reactions at the electrode surface such as hydrogen and oxygen evolution in the case of water are avoided with an inert organic solvent. With organic solvents, higher potentials (>5 V) can be used without the problems of electrolysis and joule heating.[72,73] Using conservative estimates, the temperature increase during an electrophoretic deposition experiment would be only ~0.2 K at 50 V applied.[74] However, the potentials in this study were kept low enough to avoid electrohydrodynamic instabilities and other nonlinearities. Potentials were kept below the critical voltage as given by the laminar-to-turbulent transition voltage equation[75]

(70) Overbury, S. H.; Ortiz-Soto, L.; Zhu, H.; Lee, B.; Amiridis, M. D.; Dai, S. *Catal. Lett.* **2004**, *95* (3−4), 99–106.
(71) Wang, X.; Na, N.; Zhang, S.; Wu, Y.; Zhang, X. *J. Am. Chem. Soc.* **2007**, *129* (19), 6062–6063.
(72) Van der Biest, O. O.; Vandeperre, L. J. *Annu. Rev. Mater. Sci.* **1999**, *29*, 327–352.
(73) Besra, L.; Liu, M. *Prog. Mater. Sci.* **2006**, *52* (1), 1–61.
(74) Smith, P. G., Jr.; Patel, M. N.; Kim, J.; Johnston, K. P.; Milner, T. E. *J. Phys. Chem. C* **2007**, *111* (6), 2614–2622.

$$V_{inst} = \frac{30\eta}{\sqrt{\rho\varepsilon_r\varepsilon_o}} \quad (1)$$

where η is the solvent viscosity, ρ is the solvent density, ϵ_r is the relative dielectric constant, and ϵ_o is the permittivity of free space. For chloroform, $V_{inst} = 64.5$ V ($\eta = 0.539$ cP, $\rho = 1.48$ g/mL, and $\varepsilon_r = 4.8$). Hence, the potentials applied in this study, 50 V maximum, were well below the threshold value.

The Au nanocrystals dispersed in chloroform possess an excess positive charge as the darkly colored nanocrystals were observed to accumulate near the negative electrode, while the region near the positive electrode became transparent, when an electrophoretic potential of 25 V was applied for an electrode spacing of 3 mm. While the surface charge on the Au nanocrystals was not determined quantitatively, Zheng et al. have previously reported a distribution of electrophoretic mobilities for 3.5 nm Au nanocrystals capped with dodecanethiol ligands dispersed in chloroform.[76] Roughly 85% of the nanocrystals had mobilities ranging between 0.1 and 0.5 (μm/s)/(V/cm) while a smaller percentage exhibited values from -0.2 to 0.1 (μm/s)/(V/cm). Hence, a large majority of the nanocrystals exhibit a positive charge. Since the Au nanocrystals in the present study were synthesized by similar means, a comparable distribution of mobilities and charges may be expected. Although the origin of the surface charge was not given by Zheng et al., it is possible that loss of dodecanethiol capping ligands can result in an excess positive charge on the nanocrystal.[77] The electrophoretic mobility (μ) is related to the surface charge (Q) by

$$Q = 6\pi\mu\eta a \quad (2)$$

where a is the nanocrystal radius. The reported average mobility of 0.30 (μm/s)/(V/cm)[76] translates to a surface charge of 5.4×10^{-20} C per nanocrystal or a charge of $+0.34$ per nanocrystal.

In general, the mechanism of electrophoretic deposition involves electrophoresis of particles, along with deposition on the surface.[72,78] The velocity of the nanocrystals (v) can be estimated from the measured μ of Zheng et al.[76] from the relationship

$$v = \mu E \quad (3)$$

The calculated velocities were 25 and 50 μm/s for electric fields of 83 and 170 V/cm, respectively, assuming an electrophoretic mobility of 0.30 (μm/s)/(V/cm).[76] With the electrode spacing maintained at 3 mm, the charged nanocrystals at the positive electrode would require ~120 and ~60 s, respectively, to reach the TiO_2 surface at the negative electrode. With the nanocrystals congregated at the TiO_2 film surface, the effective concentration at the film surface is greatly increased compared to the initial concentration as with the control experiment with no electric field. A kinematic shock layer[79] may form with a sharp increase in the local concentration next to the film compared to the bulk. The higher local nanocrystal concentration at the pore entrance will raise the chemical potential of the nanocrystals and thus drive adsorption.[72,78] Additionally, fluid flow around the pore opening can accelerate particle insertion into the pores,[55,80,81] although this behavior is not well-understood in organic media with large double layers. The potential drop that occurs across the pore length measured by SSPM is capable of producing electrophoresis and electro-osmosis.[56,57,82]

Haber et al. have developed a model to describe the average depth of penetration of a single particle inside a long cylindrical pore using the Fokker–Planck equation for the probability distribution.[56,57] The model takes into account the stochastic and electric field induced motion of the particle and the fluid. The electric field is aligned in the axial direction. The effects of electrophoresis, diffusion, and deposition onto the substrate may be characterized by two key numbers, the Peclet number (*Pe*, ratio of convection to diffusion) and the Damkohler number (*Da*, ratio of deposition to diffusion),[56,57] defined as

$$Pe = v_t b/D \quad (4)$$

$$Da = \kappa b/D \quad (5)$$

where v_t is the sum of the electrophoretic and electro-osmotic velocities, b is the mean pore radius, κ is the local deposition rate, and D is the diffusion coefficient. From the SSPM data, the potential drop across the film, and by assumption the pore channel, was measured to be ~1%. For a 25 V bias, the potential drop would be ~0.25 V across a pore length of 150 nm, corresponding to an electric field of ~17 kV/cm in the pore. From eq. 3, the nanocrystal electrophoretic velocity is 5.0 mm/s using an electrophoretic mobility of 0.30 (μm/s)/(V/cm),[76] and $Pe = 0.096$. With the pores closed at one end at the ITO substrate, no net volume flow exits the pore channel. Microscopic flows are possible with nonlinear velocity profiles to account for conservation of volume, but with the small pore size of only 10 nm and the low concentration of ions in the system, the electroosmotic flow is assumed to be negligible. Thus, the total velocity is given by the electrophoretic velocity, v, through the pore, and *Pe* remains 0.096.

The local deposition rate is unknown and depends upon many factors including the particle shape and size, electrostatic, van der Waals and hydrodynamic forces, as well as specific chemical interactions between Au and the substrate.[57] However, κ may be approximated from an electrophoretic model[57] given the experimental average depth of nanocrystal penetration inside the pore channel from XPS data. Assuming an average depth of the nanocrystal in the pore, z, as ~50 nm, the dimensionless mean penetration depth (χ)

(75) Novotny, V. J. Physics of Nonaqueous Colloids. In *Colloids Surfaces Reprographic Technology*; ACS Symposium Series; American Chemical Society: Washington, D.C., 1982; Vol. 200, pp 281–306.
(76) Zheng, N.; Stucky, G. D. *J. Am. Chem. Soc.* **2006**, *128* (44), 14278–14280.
(77) Evans, D. F.; Wennerstrom, H., *The Colloidal Domain: Where Physics, Chemistry, Biology, And Technology Meet*, 2nd ed.; Wiley-VCH: New York, 1999; p 632.
(78) Fukada, Y.; Nagarajan, N.; Mekky, W.; Bao, Y.; Kim, H. S.; Nicholson, P. S. *J. Mater. Sci.* **2004**, *39* (3), 787–801.
(79) Biesheuvel, P. M.; Verweij, H. *J. Am. Ceram. Soc.* **1999**, *82* (6), 1451–1455.
(80) Nadal, F.; Argoul, F.; Hanusse, P.; Pouligny, B.; Ajdari, A. *Phys. Rev. E: Stat., Nonlin., Soft Matter Phys.* **2002**, *656–1*, 061409/1–061409/8.
(81) Nadal, F.; Argoul, F.; Kestener, P.; Pouligny, B.; Ybert, C.; Ajdari, A. *Eur. Phys. J. E: Soft Matter* **2002**, *9* (4), 387–399.
(82) Gal-Or, L.; Liubovich, S.; Haber, S. *J. Electrochem. Soc.* **1992**, *139* (4), 1078–81.

$$\chi = z/(bPe) \quad (6)$$

is 105. Because the electro-osmotic velocity is assumed to be very small, we chose the lowest ratio of the electro-osmotic to electrophoretic velocity, ζ, considered in the model, $\zeta = 0.1$.[57]

Haber et al. developed a correlation to fit the results from the Fokker−Planck equation[57]

$$\chi = -\frac{1}{15} + \frac{1}{\zeta}\left(\frac{1}{3} + \frac{1}{Da}\right) \quad (7)$$

From eq 7, *Da* is approximately 0.099 given our values of χ and ζ. Thus the local deposition rate, κ, is 0.52 cm/s. This unusually small *Da* results from the extremely small pore radius, *b*. The relatively weak Au−wall specific interactions, given the high surface coverage and strong binding of the dodecanethiol ligands, and small nanocrystal radius may lower κ. For example, similar Ag nanocrystals were shown to have a dodecanethiol surface coverage of ~75%.[83] However, the Au−TiO_2 interactions were strong enough to produce reasonably high loadings even with no applied electric field ($E = 0$). The low *Da* favors relatively deep penetration of a nanocrystal inside the pore (high χ), despite the low *Pe*. The low *Pe* results from the small pore radius, *b*, and low dielectric constant, ε, which leads to a small mobility and small velocity, *v*. Upon deposition of the nanocrystal onto the negatively charged TiO_2 pore wall, charge neutralization most likely occurs.[46,47] Thus, the neutral deposited nanocrystal will not repel incoming charged nanocrystals electrostatically.

Figure 9 shows the relationship between the average depth of the nanocrystal in the pore *z* vs *P*e for various *Da* values according to eqs 6 and 7 where the pore radius $b = 5$ nm and $\zeta = 0.1$. Hence for a given *Da*, *z* is linearly proportional to *Pe* and decreases with *Da*. It is assumed that the pore length exceeds *z* and the nanocrystals do not reach the bottom. Even without an applied field, Brownian motion

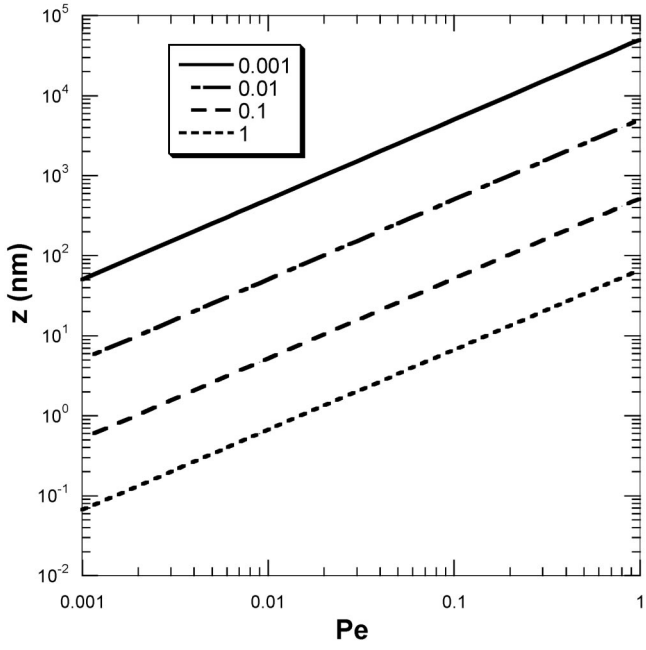

Figure 9. Average depth of penetration of a nanocrystal into a pore vs Peclet number for various Damkohler numbers assuming a pore radius $b = 5$ nm and $\zeta = 0.1$ (low electro-osmosis relative to electrophoresis).

Table 3. Kinetic Model of Average Depth of Penetration of a Single Nanocrystal into a Cylindrical Pore, Peclet Number, And Damkohler Number As a Function of Various Parameters[a]

variable	Peclet (*Pe*) (× 10^2)	Damkohler (*Da*) (× 10^2)	average depth into pore (*z*) (nm)
base case	9.6	9.9	50
pore size			
$b = 30$	29	30	160
$b = 100$	96	99	640
particle size			
$2a = 2$	6.2	6.4	50
$2a = 6$	18	19	52
electrophoretic mobility			
$\mu = 0.15$	4.8	9.9	32
$\mu = 0.60$	19	9.9	100
electric field			
$E = 8.3$	4.8	9.9	25
$E = 33$	19	9.9	100
local deposition rate constant			
$\kappa = 0.052$	9.6	0.99	490
$\kappa = 5.2$	9.6	99	6.4

[a] Base case: pore diameter $b = 10$ nm, particle diameter $2a = 3.1$ nm, electrophoretic mobility $\mu = 0.30$ (μm/s)/(V/cm), electric field $E = 17$ kV/cm, local deposition rate $\kappa = 0.52$ cm/s.

produced a significant degree of adsorption given the concentration of nanocrystals in solution. This process is not described by the Haber model; however, the addition of an electric field did increase the baseline adsorption level.

To gain more general insight into how the various factors influence the depth of penetration of a single nanocrystal into the pore, we examine the model further using eq 7 (Table 3). The base case corresponds to the parameters in this study as described above. An increase in the pore size by a factor of 3 and 10 raises the average depth, *z*, from 50 to 160 nm and 640 nm, respectively. Thus, the increase in *z* linearly correlates with the increase in *b*. Both *Pe* and *Da* increase linearly with the pore size. The average depth to pore size ratio remains constant. Small changes in the nanocrystal size have little effect on pore penetration as doubling the nanocrystal size increases *Pe* and *Da* by a factor of 2, resulting in opposing effects. The model becomes unreliable as the nanocrystal size begins to approach the pore size, and an overestimation in the average depth into the pore is likely. An increase in either μ or *E* raises v, increasing Pe and resulting in a linear increase in *z*. Even for chloroform with $\epsilon = 4.8$ and thus a relatively small μ, the electrophoretic velocity is sufficient to give deep deposition of the nanocrystals, likely because of the small κ and Da. Higher local deposition rates can be achieved by choosing different ligands during the synthesis of the nanocrystals. With weakly binding ligands and low nanocrystal surface coverage, the nanocrystal−TiO_2 surface interaction would increase. This leads to a higher local deposition rate, an increase in *Da*, and a decrease in the nanocrystal penetration depth.

For deposition of a large number of nanocrystals from solution into a pore, the single particle model describes only part of the deposition mechanism. If the first particle occupies

(83) Korgel, B. A.; Fullam, S.; Connolly, S.; Fitzmaurice, D. *J. Phys. Chem. B* **1998**, *102* (43), 8379–8388.

a site near the top of a nanopillar, the second particle may deposit onto a lower unoccupied site. The nanocrystals adsorbed on the nanopillars are less likely to block the pores than in the case of cylindrical pores. The SE results suggest that the nanocrystals did not tend to contact each other in the lateral direction. Thus the annular region about a layer of nanocrystals on each nanopillar may remain open for further particle diffusion into the pores. In addition, part of the nanocrystal's penetration into the pores may be produced by surface diffusion. The significant adsorption of nanocrystals even without an applied electric field ($E = 0$) and the large increase in loading upon doubling the bulk nanocrystal concentration (Table 2), to 12 vol % with the field present, are not addressed with the single particle model of Haber. Future work is needed to determine how changes in the binding of the ligand would influence particle−wall interactions and the adsorption and electrophoretic deposition of large numbers of particles versus pore depth.

Conclusions

Herein, we have demonstrated that 3.1 nm diameter nanocrystals can be deposited electrophoretically into ordered mesoporous TiO_2 films on ITO/glass electrodes, to reach loadings up to 21 wt %. The loadings were not limited kinetically in 10 min relative to 20 h, indicating that the open geometry of the mesochannels is beneficial for diffusion. The nanocrystals are located throughout the mesopores with only a small portion occupying the top planar surface of the film. The relatively small potential drop across the film is beneficial for electrophoretic loading of Au nanocrystals. Both VASE measurements of the anisotropy of the imaginary refractive index, k, and XPS depth profiling studies indicate that Au nanocrystals are dispersed within the vertically aligned mesopores and distributed throughout the film. Presumably, the high coverage of the strongly bound thiol ligands on the Au nanocrystals weakens the Au/TiO_2 interactions. Therefore, electrophoresis is beneficial for increasing the concentration of nanocrystals near the film, enhancing the thermodynamic driving force for adsorption of Au nanocrystals upon mesoporous TiO_2 with high loadings.

Acknowledgment. This material is based upon work supported in part by the STC Program of the National Science Foundation under Agreement CHE-9876674, the Department of Energy Office of Basic Energy Sciences, the Robert A. Welch Foundation (Grant F-1529 and F-1319), the Center for Nano and Molecular Science and Technology, and the Process Science and Technology Center at the University of Texas. R.A.M. further acknowledges the NSF for an Integrative Graduate Education and Research Traineeship (DGE-054917).

Supporting Information Available: AFM, SSPM, and UV−vis of mesoporous TiO_2 films and VASE fit parameters for Au/TiO_2 nanocomposites (PDF). This material is available free of charge via the Internet at http://pubs.acs.org.

CM8012705